Forecasting of Geomagnetically Induced Currents using Non-Linear Autoregression with Exogenous Inputs

Authors

Justice Allotey Pappoe [a,b,*], Stephen Tete [a,*], Ayman Mahrous [a]

[a] Department of Space Environment, Institute of Basic and Applied Sciences, Egypt-Japan University of Science and Technology (E-JUST), New Borg El-Arab City, Alexandria 21934, Egypt

[b] Laser and Fibre Optics Centre, School of Physical Sciences, College of Agriculture and Natural Sciences, University of Cape Coast, Cape Coast CC145, Ghana

Corresponding Author:

Justice Allotey Pappoe

justice.pappoe@ejust.edu.eg

Phone: +20 102 304 1861

Abstract

Geomagnetically induced currents (GICs) are low-frequency quasi direct currents caused by the complex interplay between Earth geomagnetic field and continuous high speed solar wind stream (HSS). The result of this interaction poses significant threats to the operations of technological infrastructures such as power grids. The integrity of oil pipelines may also be affected by the influx of GICs. As such, developing models for accurate and timely forecast of GICs is essential for mitigating the potential hazards and safeguarding valuable systems from the extreme effects of these currents. In this work, we propose a machine learning model based on the Nonlinear Autoregression with Exogenous inputs (NARX) for forecasting GICs. The model developed here forecasts GICs using inputs solely based on the solar and interplanetary parameters. The solar and interplanetary parameters retrieved from Omni Web during the maximum and minimum phases of solar cycle 23 were utilized. The developed model takes the solar wind speed, Bz, IMF, AE, ASYH, and SYMH as inputs and the measured GICs obtained from the Finnish Meteorological Institute (Mäntsälä) as the target. We validated the model using measured GICs during the geomagnetic storm periods of November 20 – 23 2003, November 7 – 13 2004 and August 24 – 26, 2005. The model's performance was evaluated using the cross-correlation coefficient (R), root-mean square error (RMSE)and the wavelet coherence analysis. The prediction accuracy for each of the individual storms are 69 %, 68 %, and 70 %, respectively. For these events, RMSEs of 1.17 A, 1.58 A and 0.56 A respectively were obtained in each case indicating the robustness of the model. The approach presented augments existing works and will contribute to the forecasting of GICs in areas where the geoelectric field and local geophysical parameters are not readily available.

Keywords:

Geomagnetically induced currents; Nonlinear Autoregression with Exogenous; Solar and interplanetary parameters; Machine learning; Artificial neural networks.

1. Introduction

GICs are known to be ground manifestations of the complicated space weather phenomena that originate from the sun (Gaunt, 2016; Lakhina et al., 2021). They are low-frequency quasi-dc currents produced as a result of the rapid changes of the Earth's geomagnetic field during solar wind-magnetosphere coupling (Dungey, 1961; Gonzalez et al., 1994). The variations of the geomagnetic fields induce surface geoelectric fields due to the telluric currents flowing through the sub-surface structure of the Earth. The geoelectric fields are mainly driven by temporal changes in the magnetic field and the local geophysical parameters (Hajra, 2022). Therefore, the intensity of GIC is related to the strength of the geoelectric field. GICs mostly flow through the conductive Earth and can cause havoc on power transmission grids, oil pipelines, telecommunication systems, and train networks. Typical examples of GICs manifestations include the disruption of telegraph operations in North America during the Carrington storm in September 1859 (Loomis, 1861), the failure of the Hydro-Québec power system in Canada caused by the storm in March 1989 (Allen et al., 1989) and the collapse of a transformer close to Malmö, Sweden, during the Halloween storm in October 2003 (Pulkkinen et al., 2005). The adverse effects caused by GICs make the ability of their effective forecast crucial to the space community, industry, and nations.

However, neither measurements of GICs nor the geoelectric field data, which is a preferable parameter for the estimate of GICs, are readily available. In the absence of available data, GICs are estimated as the derivative of ground magnetic field perturbation known as GICs proxy (Pulkkinen et al., 2013; Welling et al., 2018). Unfortunately, the GIC proxy does not substantially represent the phenomenon. This is because in the presence of the geoelectric field, GICs estimations is expressed as

$$GIC = aE_x + bE_y \tag{1}$$

where E_x and E_y represents the local geoelectric fields in the north-south and east-west components respectively. Coefficients a and b are parameters dependent on the site topology and electrical characteristics of the system. They are known to be frequency dependent (Weigel and Cilliers, 2019). From Eq. (1), it is observed that in order to achieve the best model of the GIC phenomenon, one must have a practical way to estimate the geoelectric fields as well as an understanding of the near-space environment (Pulkkinen et al., 2012). Additionally, familiarity with the local geophysical parameters of the technological system under investigation is necessary (Pulkkinen et al., 2001; Viljanen et al., 2006).

For the past decade, efforts have been made to overcome some of these pressing issues associated with estimations of GICs because information on the estimation of the geoelectric field and characteristics of the system parameters are readily not available. Several empirical models have been developed for estimating the geoelectric field perturbations (e.g., Ngwira et al., 2014; Weigel, 2003; Weimer, 2013; Wintoft, 2005; Zhang et al., 2012). Additionally, several researchers have contributed to the quest of understanding of GICs including their generation and propagation mechanisms. For example, Heyns et al., (2021) reported that long-lasting GICs can be driven by pulsation activity during corotating interaction region storms. Hajra, (2022) and Pulkkinen et al., (2001) found that the sub-auroral zone GICs occurrence is centered around local midnight due to their association with auroral activity (Akasofu and Aspnes, 1982; Campbell, 1980).

GICs hazards have socio-economic ramifications because modern civilization is becoming excessively reliant on complex electrical systems (Oughton et al., 2017). As a result, many efforts have been made to mitigate the effects of these currents through developing forecasting models that can give estimates of the levels of induced currents to expect (e.g., Bailey et al., 2022; Keesee et al., 2020; Siddique and Mahmud, 2022). Most of these models depend on the use of the geoelectric field, which are mostly not available, necessitating the use of alternate methods to derive this information. In this work, we report on a robust GICs forecasting model using ANN and information from solar and interplanetary parameters, which are readily available and easily accessible. The NARX neural network, which is a dynamic recurrent neural network, offers the needed advantage due to its ability to retain past information when applied in time-series studies.

Artificial Neural Networks (ANN) are information processing neurons that function based on the idea that basic processing units, when connected to one another in a network, can function as a unit (Pappoe et al., 2023). This kind of system mimics the functional behavior of biological neurons (Poulton, 2002). They have been utilized in different areas to solve many complex nonlinear problems (Miller, 1993; Unnikrishnan, 2014). Given that GICs are nonlinear in nature, forecasting this phenomenon requires a nonlinear approach. The NARX neural network is an ANN and one of the most well-liked approaches that has been applied in nonlinear systems, mainly because of its dynamic recurrent nature (Billings, 2013; Boaghe et al., 2001).

In space physics, NARX neural network has been utilized to model and forecast several space weather phenomena. For instance, Ayala Solares et al., (2016) employed NARX neural networks to predict the global magnetic disturbance in near-Earth space. In addition, Bhaskar and Vichare, (2019) also utilized NARX neural networks to forecast SYMH and ASYH indices

during geomagnetic storms in solar cycle 24. NARX neural networks have also been utilized to obtain the most influential coupling functions that affect the evolution of the magnetosphere (Boynton et al., 2011), and to predict the Dst index using multiresolution wavelet models (Wei, 2004). The promising results obtained from the aforementioned authors validate the use of NARX neural network for forecasting and prediction purposes. In this work, we employed the NARX neural network to explore its feasibility to forecast GICs by leveraging historical data of solar and interplanetary parameters during the maximum and minimum phases of solar cycle 23 (i.e., January 2000 to August 2005). This current paper is organized as follows: in section 2, we described the dataset used in the model development; the architecture of the NARX neural network employed in this study is described in section 3; section 4 explains the method together with reasons for our choice of inputs for the model development; the results and discussions are presented in Section 5; and Section 6 talks about the summary and conclusions made from this current study.

2. Database

The contribution of solar and interplanetary parameters is crucial for expounding on the variability of GICs. The solar and interplanetary parameters used in the current study cover January 2000 to August 2005. These years form part of the maximum and minimum phases of solar cycle 23. The high cadence (1-min resolutions) of solar wind speed, Bz, IMF, AE, ASYH, and SYMH were obtained from the Space Physics data archives of the Goddard Space Flight Center (OMNIWeb). These data are available for free to the general public for educational purposes and can be accessed from: https://omniweb.gsfc.nasa.gov/. As part of the data preprocessing phase, linear interpolation was employed to mitigate gaps in the solar and interplanetary data. The 10-s resolution GIC dataset measured at the Finnish natural oil pipeline (Mäntsäla) was used in this study. The retrieved data was resampled to 1-minute to match the resolution of the solar and interplanetary data prior to model development. The GIC dataset can be accessed through the Space and Earth Observation Center of the Finish Meteorological Institute at https://space.fmi.fi/gic/man_ascii/. Three geomagnetic storms that occurred on November 20 –23 2003, November 7 –13 2004 and August 24 –26 2005, were used to validate the model's performance. The details of these storms are presented in Section 5 of this work. A total of 1161729 datasets were obtained and used for model development. The data was divided into 80% (929383) training, 10% (116173) testing and 10% (116173) was used to validate the model. This approach of data division is necessary to ensure that the model learns the input-output relationship without suffering from overfitting. Conventionally, the validation

and testing sets are used to investigate the generalizability and performance of the model during training.

3. *NARX Neural Network*

The NARX neural network is a recurrent dynamic neural network suitable for forecasting and modelling various nonlinear systems, such as time series (Cadenas et al., 2016). A time series is a sequence of vectors depending on time, e.g., GICs. NARX consists of a Multilayer Perceptron (MLP), which takes model inputs and assigns time stamps to them, later referenced as delays for computing new output. The model architecture used in this work comprise of both open and close loops. The open-loop architecture, shown in Fig. 1 was utilized to train the model. At this stage, the training is mainly achieved from the present and true past values of the time series. The use of true past values as input gives it a major advantage. The architecture has a time-delayed feedback, *d*. As shown in Fig. 1, the input layer receives the external input values with different time lags. In addition, the past outputs (known as context inputs) are fed as inputs to the network with a history, *H*. The second layer is known as the hidden layer. In principle, the function of the hidden layer is to perform nonlinear transformations and computations on the inputs to enable the model to learn more complex tasks. The output layer is the last layer, which scales the hidden layer output to match the target.

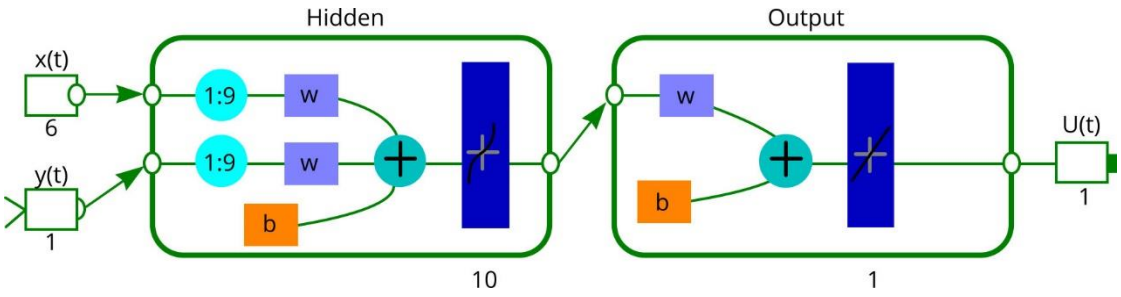

Figure 1. The open-loop NARX neural network architecture used for training the model. It consists of 6 inputs and 9 context inputs, a hidden layer with 10 neurons, and an output layer with 1 neuron representing the forecast GICs.

The mathematical equation governing the NARX model described above is expressed as

$$U_t = \psi(U_{t-1}, \dots, U_{t-H}; P_t \dots P_{t-d}) \quad (2)$$

where U_t represents the output of the network, and the input vector is denoted by P. The length of the history is denoted by H and d denotes the input history. The output of the network depends on the present, past, and history of the output, respectively. The hyperbolic tangent

function (Tansig) was utilized as the activation function purposely to introduce nonlinearity into the model. This function is expressed as

$$Z = \frac{e^{x} - e^{-x}}{e^{x} + e^{-x}} \quad (3)$$

where x represents the input vectors. After the inputs are processed by the activation function, the output of the j_{th} hidden layer node is given by:

$$F_j = tanh\left(\sum_{n=1}^{T} W_{jn} x_n + \sum_{h=1}^{H} W_{jh} C_h + b_j\right) \quad (4)$$

In Eq. (4), the value of the input node n is represented by x_n, and the total number of input nodes is T, C represents the past input, W_{jn} is a connecting weight between the input node (n) and hidden node (j), b_j is a bias of the j_{th} neuron in the hidden layer (Bhaskar and Vichare, 2019). Eq. (5) expresses the NARX network output (U(t)), which may be written as a linear summation of all outputs from hidden layer neurons and output bias b_o.

$$U(t) = \sum_{j=1}^{s} W_{oj} H_j + b_o \quad (5)$$

where the weight of the hidden node to the output node is denoted by W_{oj}, and s represents the number of hidden layer nodes.

After successfully training the network, the close-loop NARX architecture was employed in forecasting GICs. This type of NARX architecture is similar to the Feed-forward neural network (FNN) described by (Omondi et al., 2022a). In this architectural state, the inputs are fed into the hidden layer. The hidden layer nonlinearly transforms the received inputs and the output of each of the neurons in the hidden layer are sent to the output layer. The transfer function present in the output layer ensures that the network's output is similar to the input signal. In our study, the output obtained is referred to as the forecast GICs.

3.1. Network Accuracy Parameters

Three metrics, the cross-correlation coefficient (R), root-mean-square error (RMSE) and wavelet coherence were used to evaluate the model's performance. The RMSE was calculated by taking the square root of the cost function expressed in Eq. 6.

$$E = \frac{1}{N} \sum_{k=1}^{N} (T^k - O^k)^2 \quad (6)$$

where T and O are the target and output of the network, respectively and N is the total number of samples. The R, defined by Eq. 7, was used to determine the similarities between the forecast and the observed GICs.

$$R = \frac{\sum_{k=1}^{N}(T^k - \bar{T})(O^k - \bar{O})}{\sqrt{\sum_{k=1}^{N}(T^k - \bar{T})^2}\sqrt{\sum_{k=1}^{N}(O^k - \bar{O})^2}} \quad (7)$$

where $\bar{T}$ and $\bar{O}$ are the average values of target and output, respectively. All other symbols have their usual meanings as above. We utilized wavelet-based coherence analysis to study the time-frequency properties of the observed and forecast GICs. The approach employed follows the procedure described by (Omondi et al., 2022b, 2022a).

4. Method

As stated earlier, ANN forecasting comprises three steps: training, validation, and testing (Simon Haykin, 1999). The model's architecture consists of 1 input layer with 6 neurons and 9 context inputs, 1 hidden layer with 10 neurons, and 1 output layer containing 1 neuron representing the forecast GICs. This architecture was adopted due to its appreciable computation time following multiple trials. The inputs used are solar wind speed, Bz, IMF, AE, ASYH and SYMH. These parameters were chosen knowing that: (1) Intense magnetospheric compressions are associated with high solar wind speeds, which may induce stronger interactions and high energy transfer (2) The southward directed IMF favors magnetic dayside reconnection, seeds geomagnetic storms, and enhances energy transfer which drives magnetospheric currents (3) The AE index indicates the level of magnetic activity and energy transfer from the solar wind to the magnetosphere-ionosphere system. Its response is the intensification of auroral and polar region currents, which are positively associated with GICs (Akasofu and Aspnes, 1982). (4) The longitudinal symmetric (SYMH) and asymmetry (ASYH) components quantify magnetic perturbations. Enhanced reconnection at the magnetopause is manifested in the higher values of ASYH and negative excursions in SYMH, which defines the strength of the ring current. We employed GICs measured at the Finnish oil pipeline (Mäntsäla) as the target variable in this study. During the training phase, we employed the Levenberg-Marquardt back-propagation algorithm known to be the fastest and first-choice algorithm for supervised learning (Basterrech et al., 2011). Here, the weights are updated using the delta rule expressed as

$$\Delta w\ = (i\ +\ 1)\ =\ -n\frac{dE}{dw}\ +\ a.\Delta w(i) \tag{8}$$

where w denotes the weights of the nodes, i is the epoch, a and n denote momentum parameter and learning rate, respectively. The learning rate controls the learning speed, whereas the momentum parameter is used to avoid local minimums. To optimize the learning speed, n is adjusted in each iteration according to the network's performance.

5. Results and Discussion

5.1. Network Performance

The model's performance at each phase of the model development is shown in Fig. 2. The figure shows that the mean square error decreases with increasing epochs after each iteration and converges when minimal errors occur. In this work, the error given by the RMSE is 0.308 A obtained at epoch 22. Beyond this epoch, any further training might suffer from overfitting on the validation set. Conversely, when a model achieves its optimum training, the process is automatically terminated, and signaled "complete". Thus, the model is ready for independent testing on an unseen dataset. A model must have an appreciable training time to minimize computation costs and future updates as seen in Fig. 2.

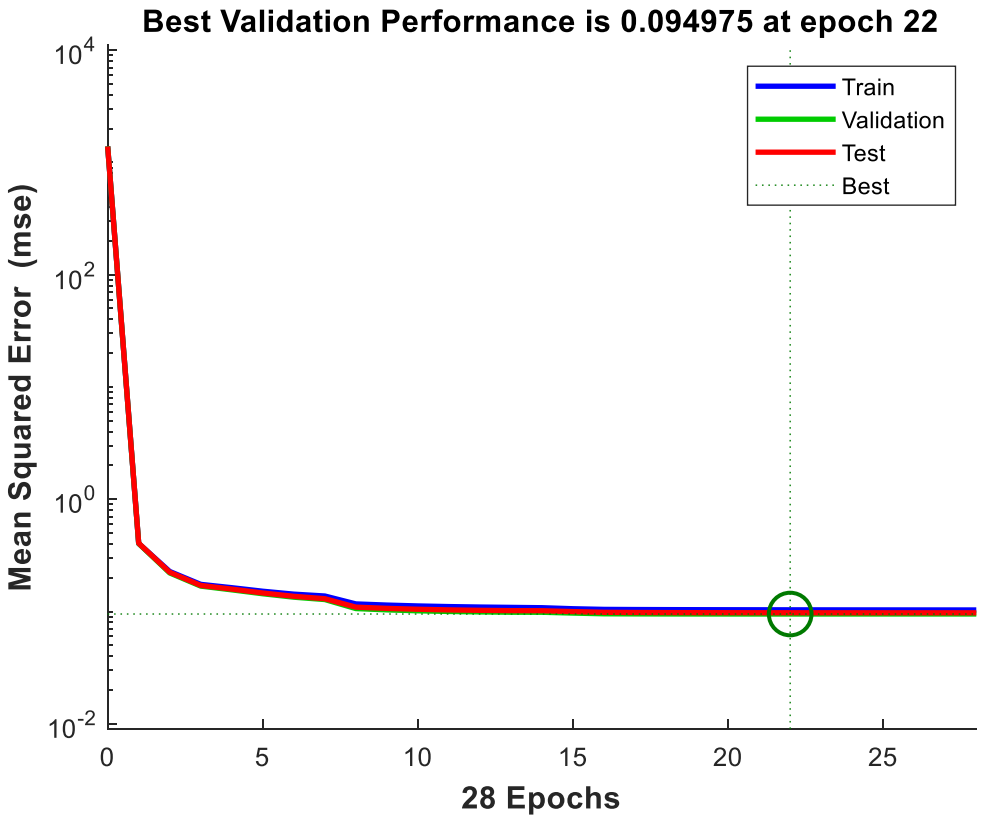

Figure 2. Training performance of the NARX neural network. The optimal point marked with a green circle with the fewest errors was obtained at epoch 22. The training, validation and testing steps have almost the same mean square error.

Fig. 3 shows the linear regression metrics between the target (observed GICs) and the model output (forecast GICs) obtained at epoch 22 during the training. The total correlation coefficient (R) obtained for the model's overall performance was 0.72. This explains a good similarity between the output and target, indicating good training accuracy.

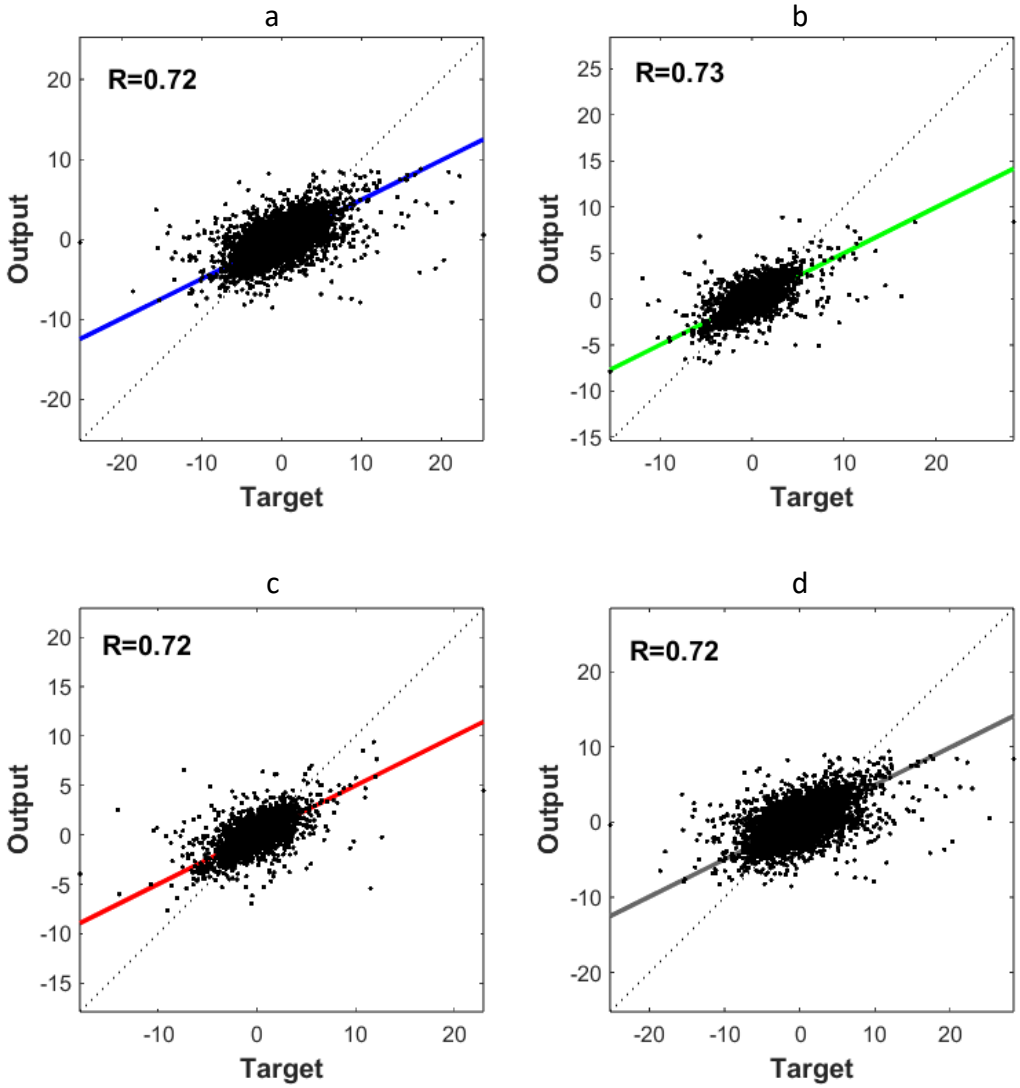

Figure 3. The linear regression metric of the target and forecast output with the line of best fit during the training phase of the model. From top to bottom; (a) represents the training, (b) represents the validation; (c) is the testing and (d) is the overall performance of the model.

5.2. Forecasting by NARX Model

The robustness of the developed model was validated using three geomagnetic storms. The intensity of the geomagnetic storms was evaluated using the SYMH (i.e., weak storm, SYMH ≥ -50 nT; moderate storm, -50 > SYMH ≥ -100 nT; intense storm, -100 > SYMH ≥ -250 nT; and super-intense storm, SYMH < -250 nT) (Gonzalez et al., 1994).

5.2.1. November 20 – 23 2003 Storm

Figure 4 shows the fluctuations in solar and interplanetary parameters and the responses observed in the forecast and the measured GICs for the storm period November 20–23, 2003. The storm's sudden commencement (SSC) (indicated with a red dashed line) was observed at around midday on 20th November 2003. The storm sudden commencement, measured by a short increase in ring current, given by the SYMH, was characterized by a sharp increase in the solar wind dynamic pressure resulting from the arrival of the wind propelled shock at the bow of the magnetosphere(Tsurutani et al., 1999). The large fluctuations observed in the Bz component (panel *a)* may be attributed to the presence of Alfvén waves (Adhikari, 2015). The southward orientation led to a dayside reconnection, resulting in charged particles damped into the magnetosphere. During this time, there was a sharp increase in the solar wind speed (panel *b)* which lasted for hours, indicating that this storm was geoeffective and mainly caused by coronal mass ejections (Goswami, 2019), evidenced by the increase in magnetic field strength field shown in (panel *c)*. The depression of the geomagnetic field due to the storm-time ring current particle enhancement (Shelley et al., 1972) is shown in (panel *d*). From this panel, it is observed that the storm was super-intense (SYMH ≤ -400 nT) (Gonzalez et al., 1994). The recovery phase of the storm, mainly characterized by a gradual increase in the SYMH, started on November 21, 2003. The high increase in ASYH (panel *e*) explains the high asymmetric response of the magnetosphere during the storm. This resulted from increased charged particles allowed to enter the magnetosphere after reconnection. As charged particles were damped into the magnetosphere, the eastward electrojet current flowing at ~ 100km was enhanced, leading to an increase in the AE index as seen in (panel *f)* (i.e., increased auroral activity) (Lemaire, 2003). Panel *g* shows the observed (blue solid lines) and forecast (red broken lines) GICs during the storm period. During the entire storm period, recorded GIC peaks were about -20 A. These high-amplitude GICs have been found to be "extreme" (Pulkkinen et al., 2001). Most

of the high-amplitude GICs were found to occur during the main phase of the storm. From the figure, it is observed that the GICs (both observed and forecast) have a good correlation with the solar and interplanetary parameters during the entire storm period.

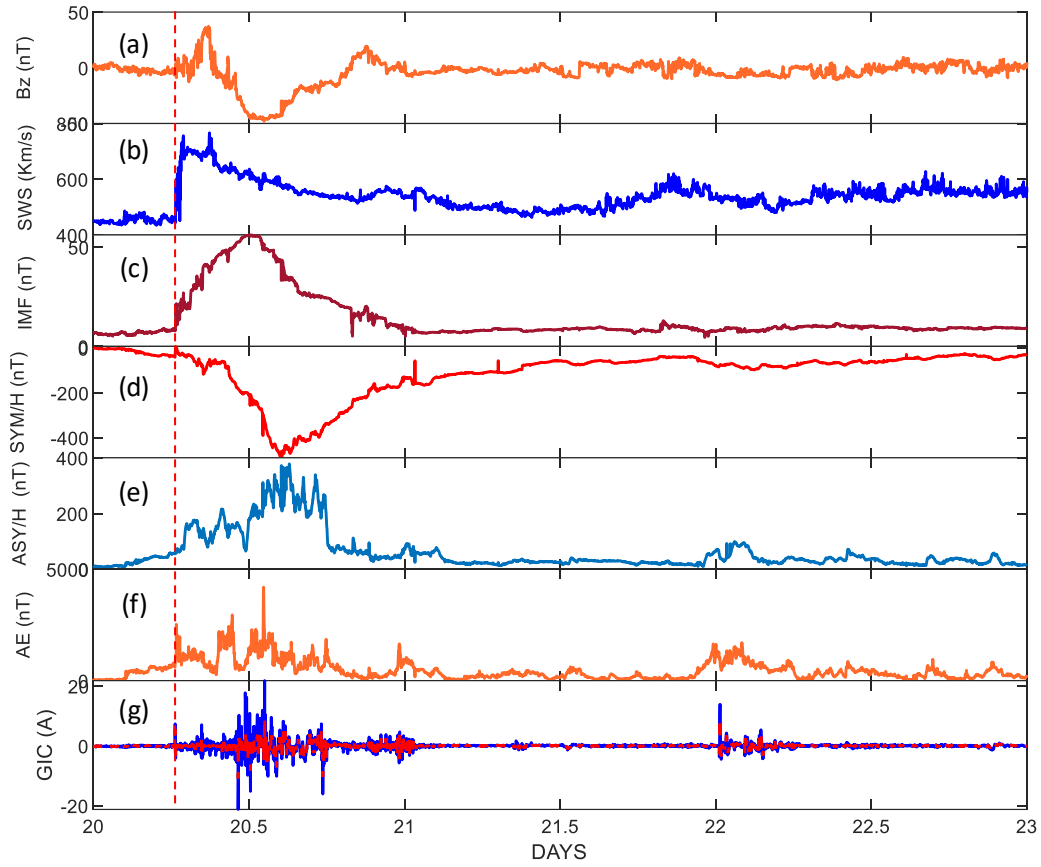

Figure 4. Solar and interplanetary parameters together with their association with observed and forecast GICs during the geomagnetic storm observed on November 20 – 23 2003. From top to bottom, panels show the fluctuations in (a) Bz, (b) solar wind speed, (c) IMF, (d) SYMH, (e) ASYH, (f) AE, and (g) GICs (observed GICs are blue colored solid lines and forecast GICs are red colored broken lines).

5.2.2. November 7 – 13 2004 Storm

Figure 5 shows the fluctuations in solar and interplanetary parameters observed during the storm on November 7 – 13 2004. Inferences from the plots follow the same pattern as described above. This storm was super-intense, with SYM-H reaching about -400 nT (Gonzalez et al., 1994). However, there were peaks of GICs that were much higher than in the previous event. The high peaks observed are resulted from the further compression of the geomagnetic field

with SYMH reaching about -250 nT (moderate storm) after the recovery of the first storm. This storm is regarded as a substorm, having an initial peak in the late hours on the 9th November, 2004 and a second peak on the 10th November, 2004. Substorms drive intense peaks of GICs due to an increased influx of particle density from the night side into the magnetosphere, which is probably the reason for the high peaks observed during this storm (Ngwira et al., 2018). A good association existed between the solar and interplanetary parameters and the observed and predicted GICs. Another interesting observation was that almost no GIC events were associated with the second excursion (SYMH ~ -280 nT) on the 10th November, 2004, which needs further discussion.

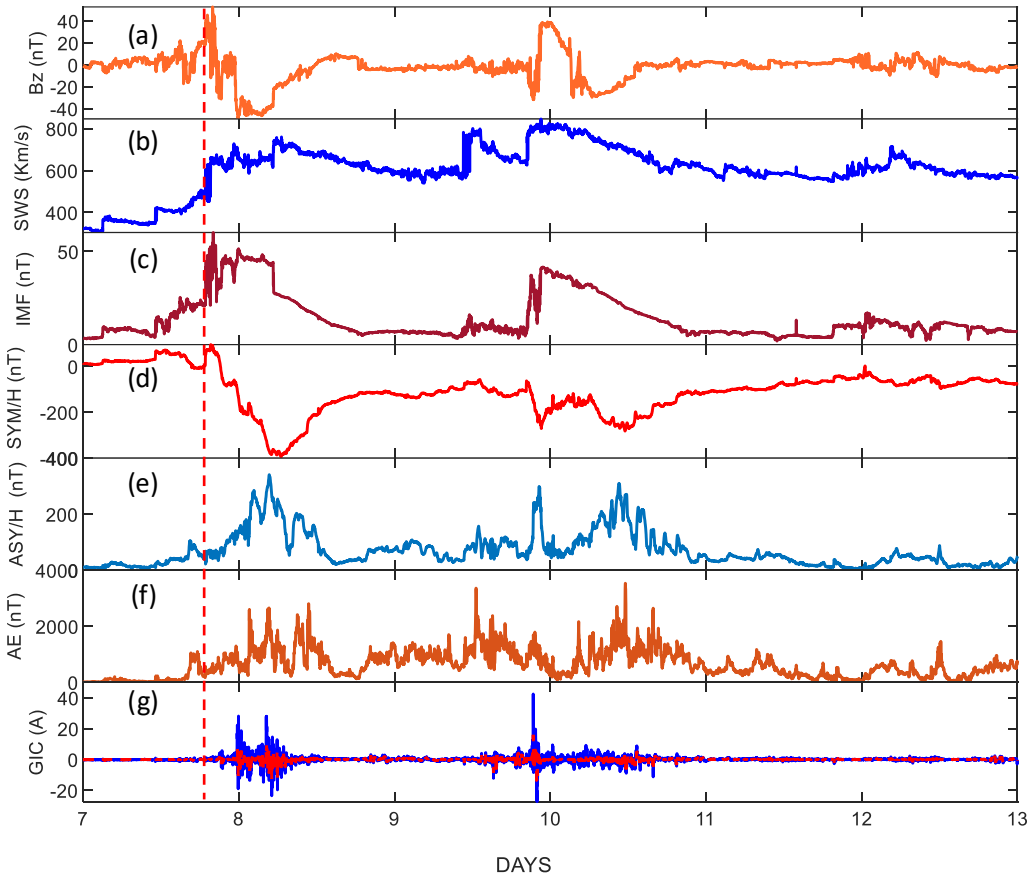

Figure 5. Solar and interplanetary parameters together with their association with observed and forecast GICs during the geomagnetic storm observed on November 7 – 13 2004. From top to bottom, panels show the fluctuations in (a) Bz, (b) solar wind speed, (c) IMF, (d) SYM-H, (e) ASY/H, (f) AE, and (g) GICs (observed GICs are blue colored solid lines and forecast GICs are red colored broken lines).

5.2.3. August 24 – 26 2005 Storm

Figure 6 shows the variation of the solar and interplanetary parameters observed during an intense storm from August 24 –26 2004. The plots follow the same pattern as described above. The storm was intense because the SYMH reached about -200 nT (Gonzalez et al., 1994). The peaks of GICs recorded during this period are very low compared to the aforementioned values. A maximum peak of 10 A was observed during this period. The low values of the peaks resulted from the storm's low strength. This validates the argument that the peak of GICs observed may be directly related to the strength of geomagnetic activity. Even though this work does not consider events on geomagnetic quiet days, we should expect very low GIC peaks on a geomagnetic quiet day compared to a geomagnetic active day.

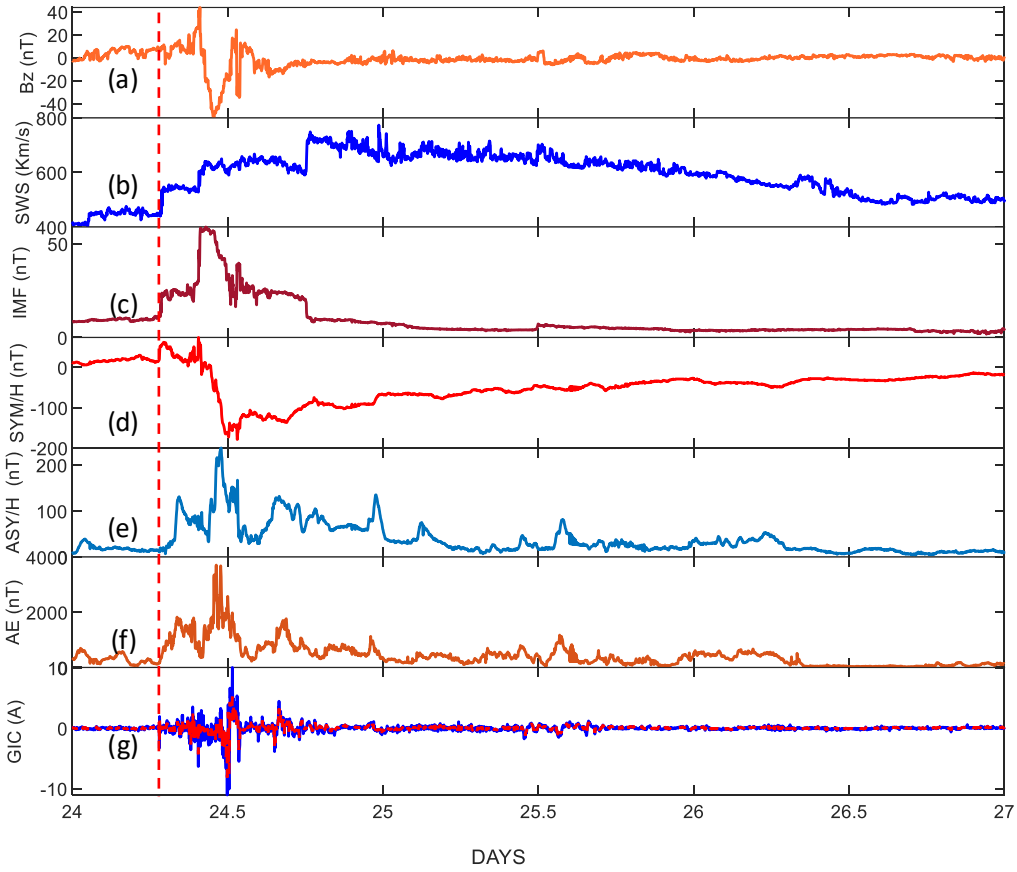

Figure 6. Solar and interplanetary parameters together with their association with observed and forecast GICs during the geomagnetic storm observed on August 24 – 26 2005. From top to bottom, panels show the fluctuations in (a) Bz, (b) solar wind speed, (c) IMF, (d) SYM-H, (e) ASY/H, (f) AE, and (g) GICs (observed GICs are blue colored solid lines and forecast GICs are red colored broken lines).

358 The forecast versus the observed GICs for the three storms is presented in Figures 7 -
359 9 respectively. The trained model forecasts the GICs with good accuracy, including the small
360 fluctuations in the peaks of the GICs. The forecast GICs look close to the observed GICs for
361 all the storms. However, it is observed that the NARX model could not forecast to a good extent
362 the large magnitude of the GICs. One possible reason for this observation is that the observed
363 GICs events may be controlled more by parameters within the magnetosphere or ionosphere
364 (Keesee et al., 2020). The results of the storm on November 20–23 2003 are presented in Fig.
365 7. Figure 7a and 7b show the wavelet analysis for both the observed and forecasted GICs
366 respectively. From 7a, the larger GIC (20th November 2003) appears to be within 0.1 to 10
367 mHz, whereas the smaller event (22nd November, 2003) was in the 0.5 to 10 mHz range. A
368 comparative analysis showed depicted the same frequency ranges for the predicted events in
369 7b. Fig. 7c, shows a time series plot for the observed and forecast GICs. A correlation of 0.69
370 and an explained variance of 0.31 were obtained. This relates to the good similarity between
371 the observed and forecast GICs. The RMSE obtained during this storm is 1.17A. We also
372 performed a wavelet coherence analysis between the observed and forecast GICs to study the
373 similarity between the two signals. For a given wavelet coherence plot, the color bar defines
374 the degree to which the two signals agree. An arrow that points to the right depicts good phase
375 coherence between the two signals. Fig. 7d shows a high coherence between both events. It is
376 also clear that the small event was adequately predicted than the larger one with degrees greater
377 than 0.8 indicating the robustness of the model.

378 Figures 8a and 8b represent the wavelet analysis of the GICs observed and forecasted
379 during the second storm on November 7–12 2004. Here, the wavelet analysis shows a good
380 similarity between the observed and forecast GIC. The two GIC events on 8th and 9th November
381 appeared in the 0.1 to 10 mHz frequency range with the same occurring for the predicted events
382 in 8b within the cone of influence (COI). The time series plot for the storm event is presented
383 in Figure 8c. The NARX model forecasted the observed GICs with a correlation accuracy of
384 0.68, having an explained variance of 0.32 with an RMSE of 1.58A. This represents a good
385 similarity between the observed and forecast GICs. Figure 8d represents the wavelet coherence
386 analysis between the observed and forecast GICs. The figure shows that there is a high
387 coherence between both events. The last storm considered for validation of this study occurred
388 on August 24th–26th, 2005. The results obtained from the NARX model are presented in
389 Figure 9. This was a single event which appeared dominant in the frequency range of about 0.2
390 to 10 mHz, as shown in the wavelet analysis plots in Figures 9a and b. The high similarity

between both GICs indicates the robustness of the NARX model. Figure 9c represents the time analysis plot for the observed and forecasted GICs. Here, the correlation between both events during the storm period was 0.70, with an explained variance of 0.30. The RMSE obtained was 0.56A.

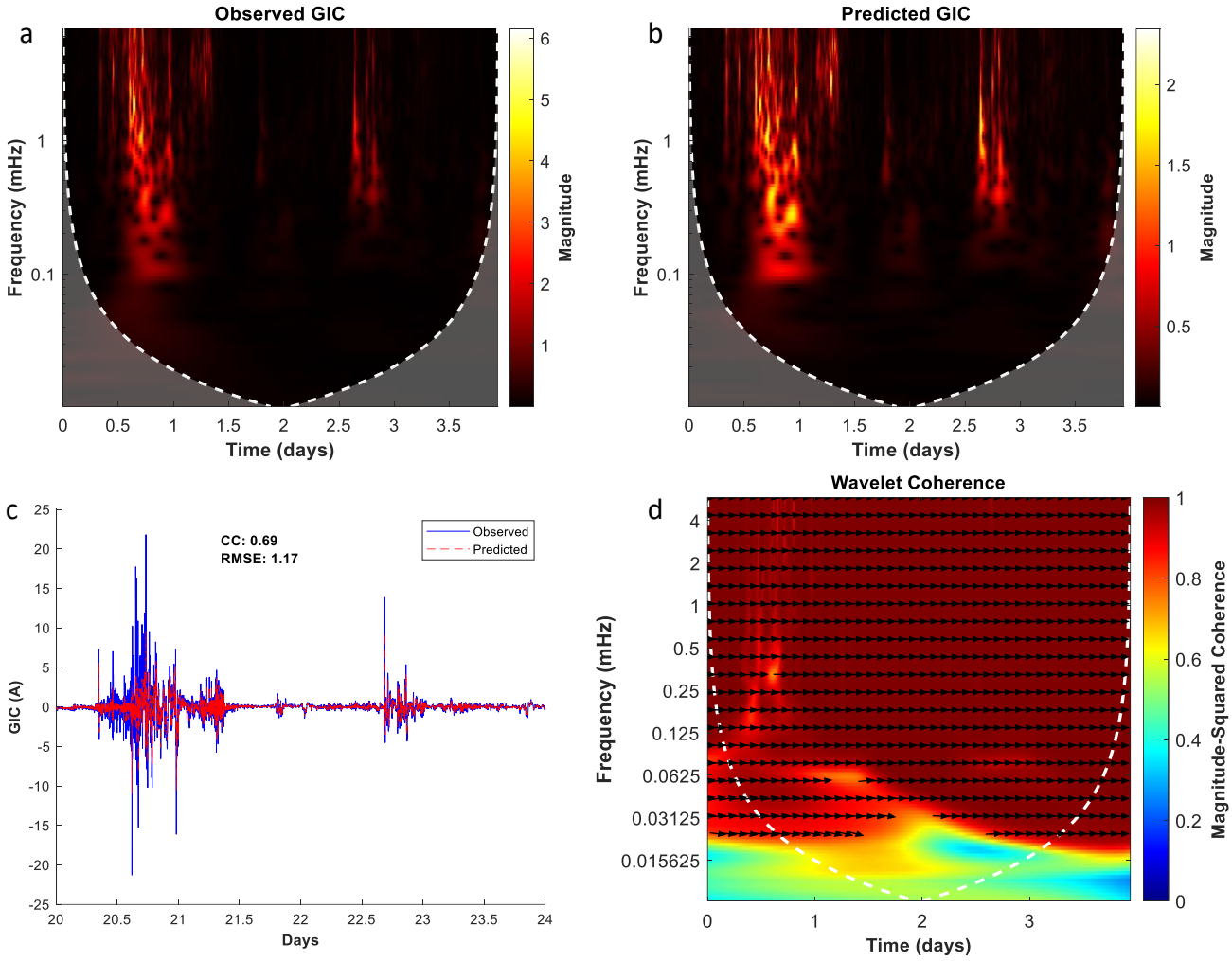

Figure 7. Forecast and observed GICs for the storm period on November 20 – 23 2003; (a) represents the wavelet analysis of the observed GIC; (b) represents wavelet analysis of forecast GIC; (c) represents the time series plot of the both the observed GICs (blue solid line) and forecast GIC (red broken line); (d) represents the wavelet coherence between both events.

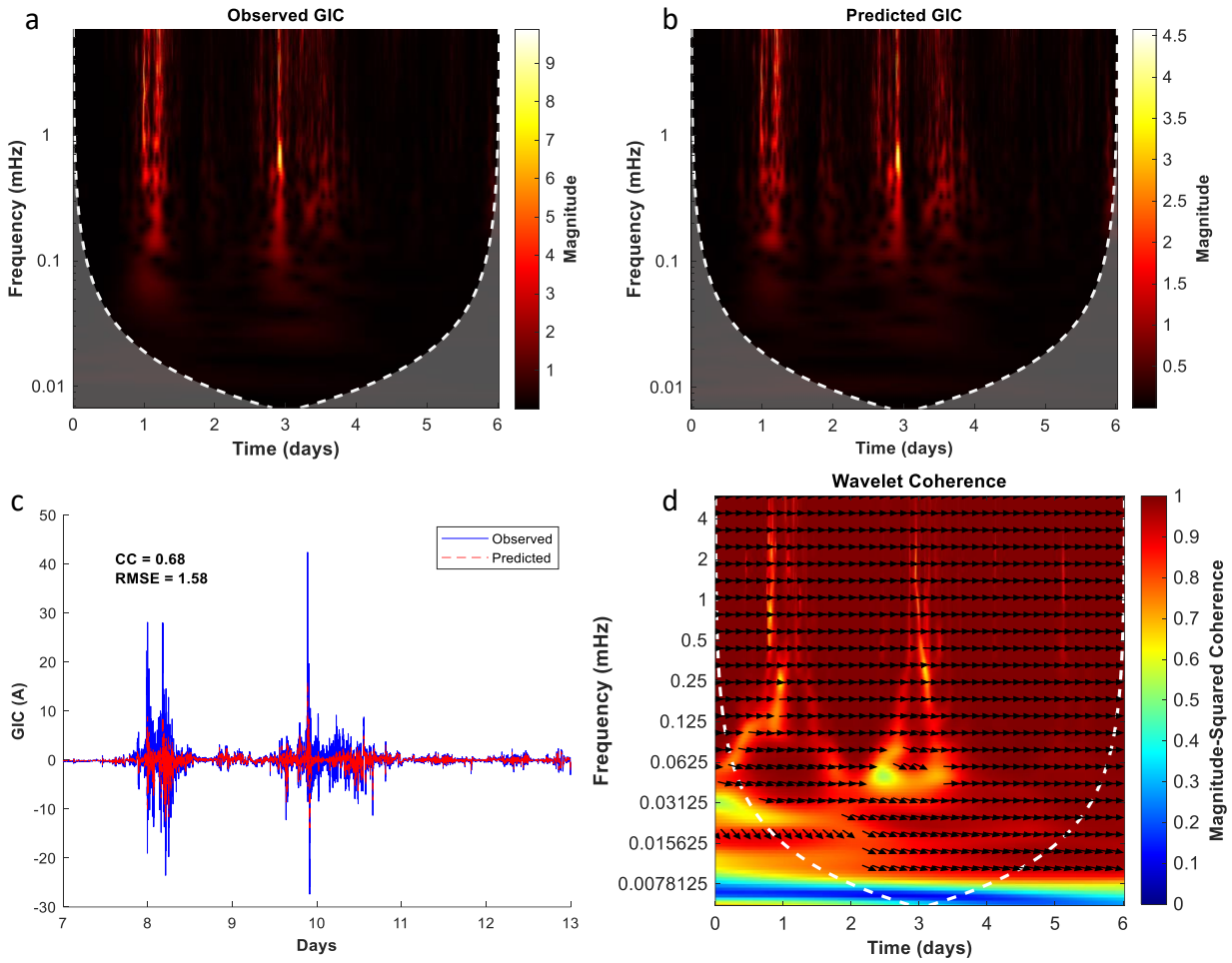

404

405 **Figure 8.** Forecast and observed GICs for the storm period on November 7 –12, 2004; (a)
406 represents the wavelet analysis of the observed GIC; (b) represents wavelet analysis of forecast
407 GIC; (c) represents the time series plot of the both the observed GICs (blue solid line) and
408 forecast GIC (red broken line); (d) represents the wavelet coherence between both events.
409

410

411

412

413

414

415

416

417

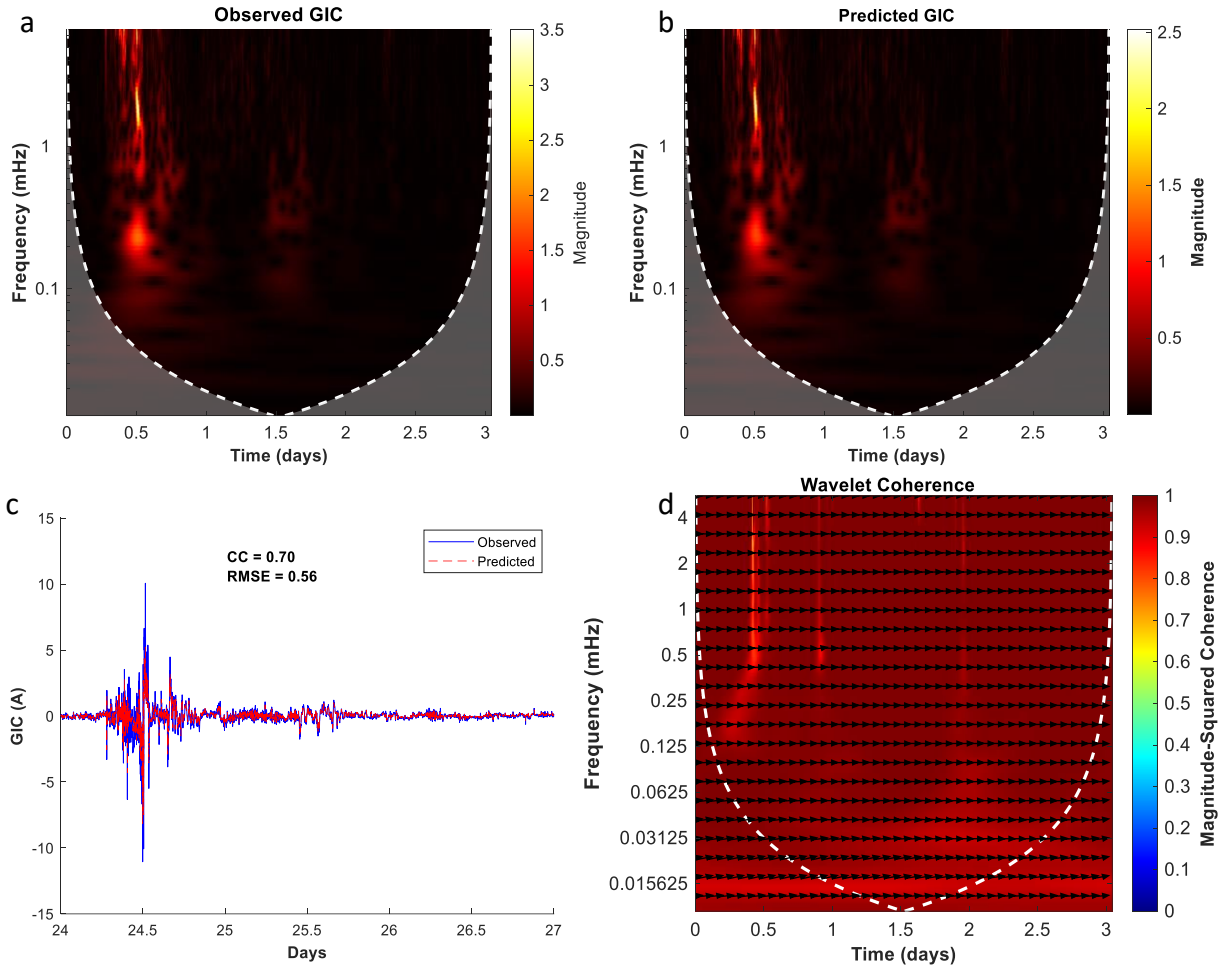

Figure 9. Forecast and observed GICs for the storm period on August 24 – 26, 2005; (a) represents the wavelet analysis of the observed GIC; (b) represents wavelet analysis of forecast GIC; (c) represents the time series plot of the both the observed GICs (blue solid line) and forecast GIC (red broken line); (d) represents the wavelet coherence between both events.

Throughout the model validations, the correlation between the observed and forecast GICs obtained is higher than the results obtained by (Keesee et al., 2020). In Keesee et al., (2020), the authors employed both feed-forward neural network and long-short term memory (LSTM) networks to forecast GICs observed at Ottawa ground magnetometer station. They obtained a forecasting accuracy of 0.66 and 0.54 respectively for the storms considered in their studies. However, the authors attributed the low correlation to the procedures employed in forecasting the geoelectric field perturbations. Meanwhile, the results obtained here are almost close to the results obtained by (Lotz et al., 2017), where the authors developed models to forecast the separate components of the horizontal magnetic field at a mid-latitude station and obtained a correlation of 0.71 and 0.69 for the GICs forecasts. The results obtained from the NARX model are similar to those obtained during the model's training, implying that the model

435 generalizes well and is consistent with the available data. In addition, the low RMSE values
436 obtained show that the model is efficient in forecasting the GICs. However, it is worth
437 mentioning that the accuracy of the NARX model decreases further depending on the storm's
438 intensity; intense storms have high accuracy compared to super intense storms. High amplitude
439 GICs have relatively low forecasting accuracy by the model compared to low amplitude GICs.

440

441 ***6. Summary and Conclusion***

442 Forecasting of GICs is a pressing problem in space weather. This is mainly because information
443 about the geoelectric field and the local geophysical parameters needed for accurate GICs
444 forecasting are not readily available. Therefore, developing an alternative means to forecast
445 GICs is crucial to help protect ground infrastructure. Researchers have tried to develop
446 alternative means to forecast GICs for some time now. However, the complexity of the subject
447 has seen just a few successes. To overcome this challenge, we developed a robust model for
448 forecasting GICs using the NARX neural network with data from some solar and interplanetary
449 parameters. This was achieved based on the good relationships between the solar and
450 interplanetary parameters and GICs. The developed model uses solar and interplanetary
451 parameters as inputs and forecast observed GICs measured at the Finnish oil pipeline
452 (Mäntsäla). The model was evaluated based on the forecasting accuracy, the RMSE and the
453 wavelet cross coherence. We validated the model using three geomagnetic storms that
454 generated GICs. The first storm was a super intense storm observed from November 20 – 23
455 2003. The NARX model forecast GICs observed during this storm with an accuracy of 69%
456 and a RMSE of 1.17 A. The second storm was also super intense observed on November 7–12
457 2004. An accuracy of 68% with a RMSE of 1.58 A was obtained during this storm. However,
458 there was a substorm after the recovery of this storm. The substorm was found to be responsible
459 for driving intense GIC peaks. The NARX model performed quite well in forecasting these
460 high peaks with appreciable errors. The last storm was an intense storm observed on August 24
461 – 26 2005. The forecasting accuracy obtained during this storm was 70% and a RMSE of 0.56
462 A. The low RMSE values showed that the model generalizes well and becomes more accurate
463 when learning from more historical datasets. In addition, we performed a wavelet coherence
464 analysis between the observed and forecast GICs. A high coherence was obtained in all storms
465 considered in the study, indicating the robustness of the developed model. The NARX model
466 developed in this work generally forecasted the observed GICs to good accuracy. However, we

concluded that the model failed to accurately forecast the high magnitudes of the GICs due to processes within the magnetosphere and ionosphere that were not captured in the present model. We also compared the forecasting accuracy obtained with other works. It was realized that the accuracies were an improvements to the work reported by (Keesee et al., 2020). On the other hand, it was almost comparable to the results obtained by (Lotz et al., 2017) in forecasting GICs. With this knowledge about the potential of ANN in the current research, it is essential that future improvements focus on assimilating even more data to enhance model's accuracy.

Acknowledgement

We acknowledge the hardworking operators of the OMNI Web database and the Finish Meteorological Institute for making the solar and interplanetary parameters and the GICs data available to the general public for scientific use. Finally, the first and second authors of this work express their gratitude to the TICAD 7 scholarship for providing funding to enable them to pursue their master degree in space environment at E-JUST.

Declaration of Competing Interest

The authors declare that the study described in this work is not influenced by any conflicting financial interests or personal relationship.

.

References

Adhikari, B., 2015. HILDCAA-related effects recorded in middle-low latitude magnetometers, PhD Thesis.

Akasofu, S.-I., Aspnes, J.D., 1982. Auroral effects on power transmission line systems. Nature 295, 136–137. https://doi.org/10.1038/295136a0

Allen, J., Sauer, H., Frank, L., Reiff, P., 1989. Effects of the March 1989 solar activity. Eos, Trans. Am. Geophys. Union 70, 1479. https://doi.org/10.1029/89EO00409

Ayala Solares, J.R., Wei, H.-L., Boynton, R.J., Walker, S.N., Billings, S.A., 2016. Modeling and prediction of global magnetic disturbance in near-Earth space: A case study for *K p* index using NARX models. Sp. Weather 14, 899–916. https://doi.org/10.1002/2016SW001463

Bailey, R.L., Leonhardt, R., Möstl, C., Beggan, C., Reiss, M.A., Bhaskar, A., Weiss, A.J., 2022. Forecasting GICs and Geoelectric Fields From Solar Wind Data Using LSTMs: Application in Austria. Sp. Weather 20, e2021SW002907. https://doi.org/10.1029/2021SW002907

Basterrech, S., Mohammed, S., Rubino, G., Soliman, M., 2011. Levenberg--Marquardt Training Algorithms for Random Neural Networks. Comput. J. 54, 125–135. https://doi.org/10.1093/comjnl/bxp101

Bhaskar, A., Vichare, G., 2019. Forecasting of SYMH and ASYH indices for geomagnetic storms of solar cycle 24 including St. Patrick's day, 2015 storm using NARX neural network. J. Sp. Weather Sp. Clim. 9, A12. https://doi.org/10.1051/swsc/2019007

Billings, S.A., 2013. Nonlinear System Identification. John Wiley & Sons, Ltd, Chichester, UK. https://doi.org/10.1002/9781118535561

Boaghe, O.M., Balikhin, M.A., Billings, S.A., Alleyne, H., 2001. Identification of nonlinear processes in the magnetospheric dynamics and forecasting of *Dst* index. J. Geophys. Res. Sp. Phys. 106, 30047–30066. https://doi.org/10.1029/2000JA900162

Boynton, R.J., Balikhin, M.A., Billings, S.A., Wei, H.L., Ganushkina, N., 2011. Using the NARMAX OLS-ERR algorithm to obtain the most influential coupling functions that affect the evolution of the magnetosphere. J. Geophys. Res. Sp. Phys. 116. https://doi.org/10.1029/2010JA015505

526 Cadenas, E., Rivera, W., Campos-Amezcua, R., Heard, C., 2016. Wind Speed Prediction Using
527 a Univariate ARIMA Model and a Multivariate NARX Model. Energies 9, 109.
528 https://doi.org/10.3390/en9020109

529 Campbell, W.H., 1980. Observation of electric currents in the Alaska oil pipeline resulting
530 from auroral electrojet current sources. Geophys. J. Int. 61, 437–449.
531 https://doi.org/10.1111/j.1365-246X.1980.tb04325.x

532 Dungey, J.W., 1961. Interplanetary Magnetic Field and the Auroral Zones. Phys. Rev. Lett. 6,
533 47–48. https://doi.org/10.1103/PhysRevLett.6.47

534 Gaunt, C.T., 2016. Why Space Weather Is Relevant to Electrical Power Systems. Sp. Weather
535 14, 2–9. https://doi.org/10.1002/2015SW001306

536 Gonzalez, W.D., Joselyn, J.A., Kamide, Y., Kroehl, H.W., Rostoker, G., Tsurutani, B.T.,
537 Vasyliunas, V.M., 1994. What is a geomagnetic storm? J. Geophys. Res. 99, 5771.
538 https://doi.org/10.1029/93JA02867

539 Goswami, A., 2019. Studying the properties of interplanetary counterpart of halo-CMEs and
540 their influences on Dst index. Adv. Sp. Res. 64, 287–298.
541 https://doi.org/10.1016/j.asr.2019.03.015

542 Hajra, R., 2022. Intense, Long-Duration Geomagnetically Induced Currents (GICs) Caused by
543 Intense Substorm Clusters. Sp. Weather 20, e2021SW002937.
544 https://doi.org/10.1029/2021SW002937

545 Heyns, M.J., Lotz, S.I., Gaunt, C.T., 2021. Geomagnetic Pulsations Driving Geomagnetically
546 Induced Currents. Sp. Weather 19, e2020SW002557.
547 https://doi.org/10.1029/2020SW002557

548 Keesee, A.M., Pinto, V., Coughlan, M., Lennox, C., Mahmud, M.S., Connor, H.K., 2020.
549 Comparison of Deep Learning Techniques to Model Connections Between Solar Wind
550 and Ground Magnetic Perturbations. Front. Astron. Sp. Sci. 7:550874.
551 https://doi.org/10.3389/fspas.2020.550874

552 Lakhina, G.S., Hajra, R., Tsurutani, B.T., 2021. Geomagnetically Induced Currents. pp. 523–
553 527. https://doi.org/10.1007/978-3-030-58631-7_245

554 Lemaire, J.., 2003. The effect of a southward interplanetary magnetic field on Störmer's
555 allowed regions. Adv. Sp. Res. 31, 1131–1153. https://doi.org/10.1016/S0273-

1177(03)00099-1

Loomis, E., 1861. On the great auroral exhibition of Aug. 28th to Sept. 4th, 1859 and on auroras generally; 8th article. Am. J. Sci. s2-32, 318–335. https://doi.org/10.2475/ajs.s2-32.96.318

Lotz, S.I., Heyns, M.J., Cilliers, P.J., 2017. Regression-based forecast model of induced geoelectric field. Sp. Weather 15, 180–191. https://doi.org/10.1002/2016SW001518

Miller, A.S., 1993. A review of neural network applications in Astronomy. Vistas Astron. 36, 141–161. https://doi.org/10.1016/0083-6656(93)90118-4

Ngwira, C.M., Pulkkinen, A., Kuznetsova, M.M., Glocer, A., 2014. Modeling extreme "Carrington-type" space weather events using three-dimensional global MHD simulations. J. Geophys. Res. Sp. Phys. 119, 4456–4474. https://doi.org/10.1002/2013JA019661

Ngwira, C.M., Sibeck, D., Silveira, M.V.D., Georgiou, M., Weygand, J.M., Nishimura, Y., Hampton, D., 2018. A Study of Intense Local d B /d t Variations During Two Geomagnetic Storms. Sp. Weather 16, 676–693. https://doi.org/10.1029/2018SW001911

Omondi, S., Yoshikawa, A., Zahra, W.K., Fathy, I., Mahrous, A., 2022a. Automatic detection of auroral Pc5 geomagnetic pulsation using machine learning approach guided with discrete wavelet transform. Adv. Sp. Res. 72, 866–883. https://doi.org/10.1016/j.asr.2022.06.063

Omondi, S., Yoshikawa, A., Zahra, W.K., Fathy, I., Mahrous, A., 2022b. Alex magnetometer and telluric station in Egypt: First results on pulsation analysis. Adv. Sp. Res. 72, 711–725. https://doi.org/10.1016/j.asr.2022.09.014

Oughton, E.J., Skelton, A., Horne, R.B., Thomson, A.W.P., Gaunt, C.T., 2017. Quantifying the daily economic impact of extreme space weather due to failure in electricity transmission infrastructure. Sp. Weather 15, 65–83. https://doi.org/10.1002/2016SW001491

Pappoe, J.A., Yoshikawa, A., Kandil, A., Mahrous, A., 2023. A machine learning approach combined with wavelet analysis for automatic detection of Pc5 geomagnetic pulsations observed at geostationary orbits. Adv. Sp. Res. https://doi.org/10.1016/j.asr.2023.11.001

Poulton, M.M., 2002. Neural networks as an intelligence amplification tool: A review of

586 applications. Geophysics 67, 979–993. https://doi.org/10.1190/1.1484539

587 Pulkkinen, A., Bernabeu, E., Eichner, J., Beggan, C., Thomson, A.W.P., 2012. Generation of
588 100-year geomagnetically induced current scenarios. Sp. Weather 10, S04003.
589 https://doi.org/10.1029/2011SW000750

590 Pulkkinen, A., Lindahl, S., Viljanen, A., Pirjola, R., 2005. Geomagnetic storm of 29-31
591 October 2003: Geomagnetically induced currents and their relation to problems in the
592 Swedish high-voltage power transmission system. Sp. Weather 3, S08C03.
593 https://doi.org/10.1029/2004SW000123

594 Pulkkinen, A., Pirjola, R., Boteler, D., Viljanen, A., Yegorov, I., 2001. Modelling of space
595 weather effects on pipelines. J. Appl. Geophys. 48, 233–256.
596 https://doi.org/10.1016/S0926-9851(01)00109-4

597 Pulkkinen, A., Rastätter, L., Kuznetsova, M., Singer, H., Balch, C., Weimer, D., Toth, G.,
598 Ridley, A., Gombosi, T., Wiltberger, M., Raeder, J., Weigel, R., 2013. Community-wide
599 validation of geospace model ground magnetic field perturbation predictions to support
600 model transition to operations. Sp. Weather 11, 369–385.
601 https://doi.org/10.1002/swe.20056

602 Shelley, E.G., Johnson, R.G., Sharp, R.D., 1972. Satellite observations of energetic heavy ions
603 during a geomagnetic storm. J. Geophys. Res. 77, 6104–6110.
604 https://doi.org/10.1029/JA077i031p06104

605 Siddique, T., Mahmud, M.S., 2022. Ensemble deep learning models for prediction and
606 uncertainty quantification of ground magnetic perturbation. Front. Astron. Sp. Sci. 9.
607 https://doi.org/10.3389/fspas.2022.1031407

608 Simon Haykin, 1999. Neural Networks, A Comprehensive Foundation, 2nd ed. Upper Saddle
609 River, N.J. : Prentice Hall, New Jersey, USA.

610 Tsurutani, B.T., Gonzalez, W.D., Kamide, Y., Ho, C.M., Lakhina, G.S., Arballo, J.K., Thorne,
611 R.M., Pickett, J.S., Howard, R.A., 1999. The interplanetary causes of magnetic storms,
612 HILDCAAs and viscous interaction. Phys. Chem. Earth, Part C Solar, Terr. Planet. Sci.
613 24, 93–99. https://doi.org/10.1016/S1464-1917(98)00014-2

614 Unnikrishnan, K., 2014. Prediction of horizontal component of earth's magnetic field over
615 Indian sector using neural network model. J. Atmos. Solar-Terrestrial Phys. 121, 206–

220. https://doi.org/10.1016/j.jastp.2014.06.014

Viljanen, A., Pulkkinen, A., Pirjola, R., Pajunpää, K., Posio, P., Koistinen, A., 2006. Recordings of geomagnetically induced currents and a nowcasting service of the Finnish natural gas pipeline system. Sp. Weather 4, S10004. https://doi.org/10.1029/2006SW000234

Wei, H.L., 2004. Prediction of the *Dst* index using multiresolution wavelet models. J. Geophys. Res. 109, A07212. https://doi.org/10.1029/2003JA010332

Weigel, R.S., 2003. Solar wind coupling to and predictability of ground magnetic fields and their time derivatives. J. Geophys. Res. 108, 1298. https://doi.org/10.1029/2002JA009627

Weigel, R.S., Cilliers, P.J., 2019. An Evaluation of the Frequency Independence Assumption of Power System Coefficients Used in Geomagnetically Induced Current Estimates. Sp. Weather 17, 1674–1688. https://doi.org/10.1029/2019SW002234

Weimer, D.R., 2013. An empirical model of ground-level geomagnetic perturbations. Sp. Weather 11, 107–120. https://doi.org/10.1002/swe.20030

Welling, D.T., Ngwira, C.M., Opgenoorth, H., Haiducek, J.D., Savani, N.P., Morley, S.K., Cid, C., Weigel, R.S., Weygand, J.M., Woodroffe, J.R., Singer, H.J., Rosenqvist, L., Liemohn, M.W., 2018. Recommendations for Next-Generation Ground Magnetic Perturbation Validation. Sp. Weather 16, 1912–1920. https://doi.org/10.1029/2018SW002064

Wintoft, P., 2005. Study of the solar wind coupling to the time difference horizontal geomagnetic field. Ann. Geophys. 23, 1949–1957. https://doi.org/10.5194/angeo-23-1949-2005

Zhang, J.J., Wang, C., Tang, B.B., 2012. Modeling geomagnetically induced electric field and currents by combining a global MHD model with a local one-dimensional method. Sp. Weather 10, S05005. https://doi.org/10.1029/2012SW000772